Coulomb excitations in AA- and AB-stacked bilayer graphites

J. H. Ho,[1] C. L. Lu,[2] C. C. Hwang,[2] C. P. Chang,[3] and M. F. Lin[1]

[1]*Department of Physics, National Cheng Kung University, Taiwan*
[2]*Department of Engineering Science, National Cheng Kung University, Taiwan*
[3]*Center for General Education, Tainan Woman's College of Art and Technology, Taiwan*

The π-electronic excitations are studied for the AA- and AB-stacked bilayer graphites within the linear self-consistent-field approach. They are strongly affected by the stacking sequence, the interlayer atomic interactions, the interlayer Coulomb interactions, and the magnitude of the transferred momentum. However, they hardly depend on the direction of the transferred momentum and the temperature. There are three low-frequency plasmon modes in the AA-stacked system but not the AB-stacked system. The AA- and AB-stacked plasmons exhibit the similar π plasmons. The first low-frequency plasmon behaves as an acoustic plasmon, and the others belong to optical plasmons. The bilayer graphites quite differ from the monolayer graphite and the AB-stacked bulk graphite, such as the low-frequency plasmons and the small-momentum π plasmons.

I. INTRODUCTION

The layered graphites are one of the most extensively studied materials experimentally[1–11] and theoretically.[12–21] The bulk graphite, with infinite layers, is a semimetal because of the weak van der Waals interactions between neighboring layers. The free carriers due to the band overlap could induce rich physical properties: e.g., electronic excitations,[3,4,6–8] optical spectra,[5,9] and transport properties.[10,11] Recently, monolayer, dilayer, and trilayer graphites have been produced by mechanical friction.[22–24] These few-layer graphites are very stable, mainly owing to the strong σ bonding in the plane. They are very suitable for studies of two-dimensional phenomena. Measurements of magnetotransport properties show that the few-layer graphites display the novel quantum Hall effect.[25,26] A monolayer graphite could be further reduced to one-dimensional (1D) or 0D nanographite ribbons.[27,28] Moreover, atoms or molecules could be intercalated or doped into the graphitic systems.[29] The rich geometric structures would be directly reflected in the essential physical properties. In this work, we mainly study the π-electronic excitations of the AA- and AB-stacked bilayer graphites. Electronic excitations, which are one of the essential many-particle properties, are useful in understanding the effective Coulomb interactions between electrons in the same or different layers. The dependence of excitation properties on the interlayer atomic interactions, the interlayer Coulomb interations, the stacking sequence, the temperature, and the magnitude and direction of the transferred momentum (**q**) is investigated in detail. Comparison with the monolayer graphite and the AB-stacked bulk graphite is also made.

The $2p_z$ orbitals in the AB-stacked bulk graphite could form the π bands.[13,14] The valence and conduction bands overlap each other by interlayer atomic interactions. The low-energy carriers could exhibit low-frequency plasmons with ω_p's smaller than 0.2 eV.[3–5,18] All π electrons display another kind of plasmons: π plasmons with ω_p's larger than 6.5 eV.[6–9] The low-frequency plasmons are very sensitive to the change in temperature, while the opposite is true for the

π plasmons. Both kinds of plasmons belong to optical plasmons, and they had been verified by electron-energy-loss spectroscopy[3,4,6–8] (EELS) and optical spectroscopy.[5,9] Whether they could exist in the few-layer graphites would be studied in detail.

A monolayer graphite owns hexagonal symmetry so that there exist a linear valence band and conduction band just intersecting at the Fermi level.[12] The 2D density of states is vanishing at $E_F = 0$; therefore, a monolayer graphite is a zero-gap semiconductor. The free carriers are absent at $T = 0$ and so are the low-frequency plasmons. The temperature could induce some free electrons and holes. From the previous work,[17] a monolayer graphite is predicted to be the first undoped system which could exhibit the low-frequency plasmons purely due to temperature.

We use the $2p_z$ tight-binding model to calculate the π bands of AA- and AB-stacked bilayer graphites. The loss function, which characterizes the intrinsic excitation properties, is derived within the linear self-consistent-field[30] (SCF) method. For the Coulomb excitations of the multilayered systems, this work is a theoretical study where interlayer atomic interactions and interlayer Coulomb interactions are taken into account simultaneously. Such interactions could make the bilayer graphites exhibit rich excitation properties, such as various single-particle excitations and loss spectra. The bilayer graphites are very different from the bulk graphite and the monolayer graphite in the low-frequency plasmons and the π plasmons. The predicted single-particle spectra and plasmons could be examined by EELS and optical experiments.

This paper is organized as follows. The π-electronic structures and the loss functions of the bilayer graphites are derived in Sec. II. The main characteristics of the π-electronic excitations are discussed in Sec. III. Finally, Sec. IV contains concluding remarks.

II. TIGHT-BINDING MODEL AND THE LINEAR SCF METHOD

The geometric structure of the AA-stacked bilayer graphite is shown in Fig. 1(a). Carbon atoms in two layers have
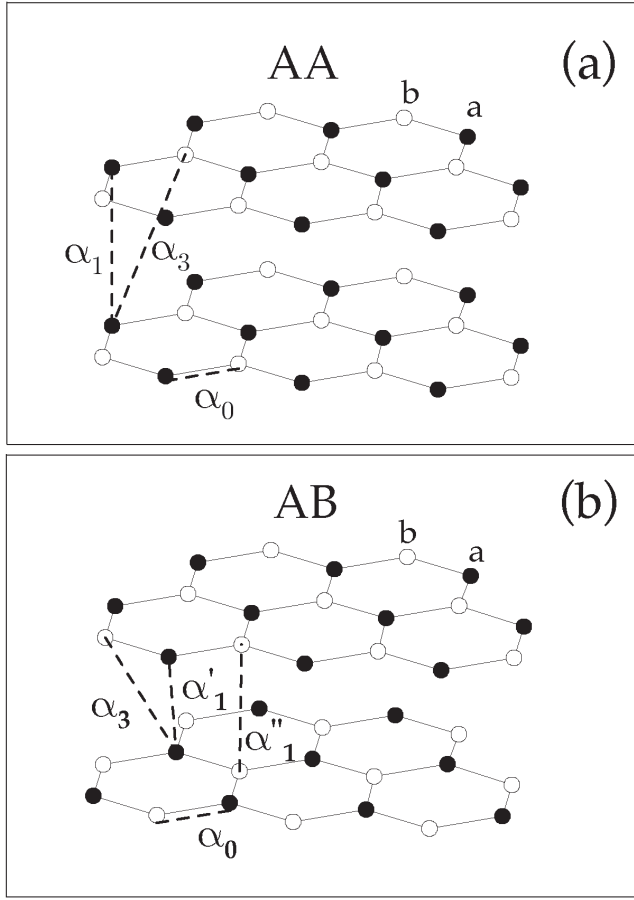
FIG. 1. The geometric structures of the (a) AA- and (b) AB-stacked bilayer graphites. The intralayer and interlayer atomic interactions are also shown.

identical (x,y) coordinates, and the interlayer distance is I_c $=3.35$ Å. There are four carbon atoms in a primitive cell. The four tight-binding functions are represented by $U_{1a}(\mathbf{k})$, $U_{1b}(\mathbf{k})$, $U_{2a}(\mathbf{k})$, and $U_{2b}(\mathbf{k})$. The Hamiltonian, which is built from the subspace spanned by these functions, is a 4×4 Hermitian matrix

$$H_{\mathbf{k}} = \begin{pmatrix} 0 & -\alpha_0 h_{\mathbf{k}} & -\alpha_1 & -\alpha_3 h_{\mathbf{k}} \\ -\alpha_0 h_{\mathbf{k}}^* & 0 & -\alpha_3 h_{\mathbf{k}}^* & -\alpha_1 \\ -\alpha_1 & -\alpha_3 h_{\mathbf{k}} & 0 & -\alpha_0 h_{\mathbf{k}} \\ -\alpha_3 h_{\mathbf{k}}^* & -\alpha_1 & -\alpha_0 h_{\mathbf{k}}^* & 0 \end{pmatrix}, \quad (1)$$

where $h_{\mathbf{k}} = \Sigma_{j=1}^3 \exp(-i\mathbf{k} \cdot \mathbf{r}_j)$ and $\mathbf{r}_j$ is the position vector of the nearest-neighbor b atom measured from the a atom. The chemical environment is the same for a atom and b atom, so the site energies are set to zero. The nonvanishing off-diagonal matrix elements[13,14] $\alpha_0=2.569$ eV, $\alpha_1=0.361$ eV, and $\alpha_3=-0.032$ eV, respectively, represent the atomic hopping integrals between two nearest-neighbor atoms in the same layer, between two a atoms from two different layers, and between a atom and b atom from two neighboring layers. Energy dispersions of the AA-stacked bilayer graphite are obtained from diagonalizing the Hamiltonian

$$E_n(\mathbf{k}) = -\alpha_1 \pm (\alpha_0 + \alpha_3)|h_{\mathbf{k}}|; \quad \alpha_1 \pm (\alpha_0 - \alpha_3)|h_{\mathbf{k}}|, \quad (2)$$

and the wave functions are

$$\Psi_{n\mathbf{k}} = \frac{1}{2}\left\{ U_{1a}(\mathbf{k}) \mp \frac{h_{\mathbf{k}}^*}{|h_{\mathbf{k}}|} U_{1b}(\mathbf{k}) + U_{2a}(\mathbf{k}) \mp \frac{h_{\mathbf{k}}^*}{|h_{\mathbf{k}}|} U_{2b}(\mathbf{k}) \right\},$$

$$\frac{1}{2}\left\{ -U_{1a}(\mathbf{k}) \pm \frac{h_{\mathbf{k}}^*}{|h_{\mathbf{k}}|} U_{1b}(\mathbf{k}) + U_{2a}(\mathbf{k}) \mp \frac{h_{\mathbf{k}}^*}{|h_{\mathbf{k}}|} U_{2b}(\mathbf{k}) \right\}. \quad (3)$$

$E_n(\mathbf{k})$ in Eq. (2) becomes that $(\pm\alpha_0|h_{\mathbf{k}}|)$ of a monolayer graphite for $\alpha_1=\alpha_3=0$.

Similar band-structure calculations are done for the AB-stacked bilayer graphite. When one layer is moved along the armchair direction with the C-C bond length 1.42 Å [Fig. 1(b)], its (x,y) coordinates are identical to those of another layer. The intralayer nearest-neighbor atomic interactions are characterized by $\alpha_0=2.598$ eV.[13,14] The interlayer atomic hopping integrals are, respectively, $\alpha_1'=0.364$ eV for two a atoms, $\alpha_1''=0.319$ eV for two b atoms, and $\alpha_3=0.177$ eV for a atom and b atom. Since a atom and b atom have different chemical environments, the difference in the site energy is characterized by $\alpha_6=-0.026$ eV. The Hamiltonian matrix associated with the four tight-binding functions is given by

$$H_{\mathbf{k}} = \begin{pmatrix} \alpha_6 & -\alpha_0 h_{\mathbf{k}} & -\alpha_1' & -\alpha_3 h_{\mathbf{k}}^* \\ -\alpha_0 h_{\mathbf{k}}^* & 0 & -\alpha_3 h_{\mathbf{k}}^* & -\alpha_1'' h_{\mathbf{k}} \\ -\alpha_1' & -\alpha_3 h_{\mathbf{k}} & \alpha_6 & -\alpha_0 h_{\mathbf{k}}^* \\ -\alpha_3 h_{\mathbf{k}} & -\alpha_1'' h_{\mathbf{k}}^* & -\alpha_0 h_{\mathbf{k}} & 0 \end{pmatrix}. \quad (4)$$

Equation (4) does not have analytic solutions for the π-electronic structures. The wave functions are the linear superposition of the four tight-binding functions—i.e., $\Psi_n(\mathbf{k})=\Sigma_{li}u_{nli}(\mathbf{k})U_{li}(\mathbf{k})$ ($l=1$, 2 and $i=a$, b).

The interlayer atomic interactions and the stacking sequence dominate the π-electronic structure. A monolayer graphite has the linear valence band (π) and conduction band (π^*) intersecting at the Fermi level ($E_F=0$) or the K point. Energy bands are isotropic only near the K point [the corner of the first Brillouin zone, as shown in Fig. 2(a)]. The M point, with energies $\pm\alpha_0$, is the critical point in the energy-wave-vector space. The Γ point, which corresponds to the maximum and minimum, determines the π-band width. The four low-energy bands of the AA-stacked bilayer graphite, as shown in the inset of Fig. 2(a), are linear and almost isotropic near the K point. Their slopes $[3(\alpha_0\pm\alpha_3)b/2$ in Eq. (2)] are very close to that $(3\alpha_0 b/2)$ of a monolayer graphite. These energy bands intersect one another, and the Fermi momenta are changed from the K point to the neighboring points. Free electrons and holes, respectively, exist in the π_1 band and π_1^* band. States energies of the M point are lowered or raised by the interlayer atomic interactions. Concerning the AB-stacked bilayer graphite, the interlayer atomic interactions make linear bands become parabolic bands, as shown in the inset of Fig. 2(b). The lowest valence band and conduction band only have a weak overlap near the K point; that is, the density of free carriers is very low. Another pair of
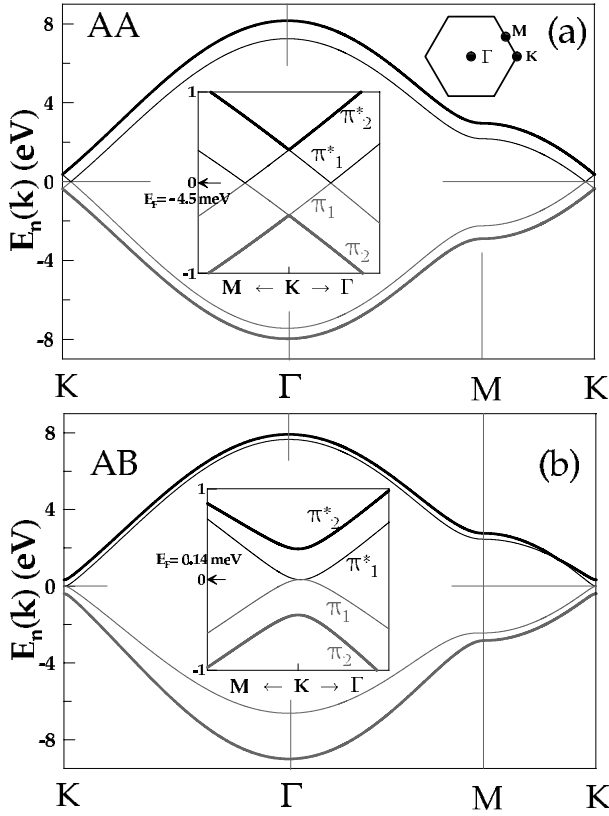
FIG. 2. The π-electron structures of the (a) AA- and (b) AB-stacked bilayer graphites.

parabolic bands have a energy spacing $(2\alpha_1')$ at the K point. The significant changes of band structures would be directly reflected in excitation properties.

The electron-electron (e-e) Coulomb interactions would induce charge screening and thus dominates excitation properties. The total Hamiltonian with the e-e Coulomb interactions is

$$H = \sum_{\mathbf{k}n} E_n(\mathbf{k})C_{n\mathbf{k}}^\dagger C_{n\mathbf{k}} + \frac{1}{2}\sum_{\mathbf{k}_1\mathbf{k}_2\mathbf{q}}\sum_{n_1n_1'}\sum_{n_2n_2'} V(q,(n_1,n_1'),(n_2,n_2'))$$
$$\times C_{n_1'\mathbf{k}_1+\mathbf{q}}^\dagger C_{n_2'\mathbf{k}_2-\mathbf{q}}^\dagger C_{n_2\mathbf{k}_2}C_{n_1\mathbf{k}_1}. \tag{5}$$

The momentum transfer $\mathbf{q}$ is conserved during the e-e Coulomb interactions. $\mathbf{q}=[q\cos\phi, q\sin\phi]$, where ϕ is the direction of the transferred momentum relative to ΓK. The wave functions are composed of the four tight-binding functions; therefore, $V(q,(n_1,n_1'),(n_2,n_2'))$ includes the interlayer and intralayer Coulomb interactions. The interlayer Coulomb interactions are proportional to the product of the 2D bare Coulomb potential $v_q e^{-ql_c}$ and the Coulomb matrix element:

$$\langle U_{1i}(\mathbf{k}_1+\mathbf{q})|e^{i\mathbf{q}\cdot\mathbf{r}_1}|U_{1i}(\mathbf{k}_1)\rangle\langle U_{2i'}(\mathbf{k}_2-\mathbf{q})|e^{-i\mathbf{q}\cdot\mathbf{r}_2}|U_{2i'}(\mathbf{k}_2)\rangle$$
$$= I^2(q), \tag{6}$$

where $v_q = 2\pi e^2/q$ and $I(q) = (1+q^2/36)^{-3}$.[15,16] As to the intralayer Coulomb interactions, the bare Coulomb potential is v_q and the two tight-binding functions are the same in the Coulomb matrix element. All the overlap integrals between

neighboring atoms, as done for band structure,[12] are neglected in the two-particle Coulomb matrix elements.

The π-electronic excitations of the bilayer graphites could be measured by the probing electrons with time-dependent potentials. The density distribution of the probing electrons is assumed to be uniform inside the bilayer systems. The perturbation potentials include $V_{11}=V_{22}=v_q$ and $V_{12}=V_{21}=v_q e^{-ql_c}$. The π electrons on two layers will screen these external potentials, which, thus, causes the induced charges. The effective potentials (V^{eff}'s) are the sum of the external potentials and the induced potentials from all the screening charges. The four linear response equations within the SCF method could be expressed as the matrix form

$$\begin{pmatrix} V_{11}(q) & V_{12}(q) \\ V_{21}(q) & V_{22}(q) \end{pmatrix}$$
$$= \begin{pmatrix} \epsilon_{11}(\mathbf{q},\omega) & \epsilon_{12}(\mathbf{q},\omega) \\ \epsilon_{21}(\mathbf{q},\omega) & \epsilon_{22}(\mathbf{q},\omega) \end{pmatrix}\begin{pmatrix} V_{11}^{eff}(\mathbf{q},\omega) & V_{12}^{eff}(\mathbf{q},\omega) \\ V_{21}^{eff}(\mathbf{q},\omega) & V_{22}^{eff}(\mathbf{q},\omega) \end{pmatrix}, \tag{7}$$

where the dielectric function in the matrix form is given by

$$\begin{pmatrix} \epsilon_{11}(\mathbf{q},\omega) & \epsilon_{12}(\mathbf{q},\omega) \\ \epsilon_{21}(\mathbf{q},\omega) & \epsilon_{22}(\mathbf{q},\omega) \end{pmatrix}$$
$$= \begin{pmatrix} \epsilon_0 - \sum_l V_{1l}(q)P_{l1}^{(1)}(\mathbf{q},\omega) & -\sum_l V_{1l}(q)P_{l2}^{(1)}(\mathbf{q},\omega) \\ -\sum_l V_{2l}(q)P_{l1}^{(1)}(\mathbf{q},\omega) & \epsilon_0 - \sum_l V_{2l}(q)P_{l2}^{(1)}(\mathbf{q},\omega) \end{pmatrix}, \tag{8}$$

$\epsilon_0 = 2.4$ is the background dielectric constant.[15,16] The summation terms on the right-hand side of Eq. (8) are associated with the induced potentials. The linear bare response function is given by

$$P_{ll'}^{(1)}(\mathbf{q},\omega) = 2\sum_{\mathbf{k}}\sum_{nn'}\left(\sum_i u_{nli}(\mathbf{k})u_{n'li}^*(\mathbf{k}+\mathbf{q})\right)$$
$$\times\left(\sum_{i'} u_{nl'i'}^*(\mathbf{k})u_{n'l'i'}(\mathbf{k}+\mathbf{q})\right)$$
$$\times\frac{f(E_n(\mathbf{k})) - f(E_{n'}(\mathbf{k}+\mathbf{q}))}{E_n(\mathbf{k}) - E_{n'}(\mathbf{k}+\mathbf{q}) + \hbar\omega + i\Gamma}. \tag{9}$$

The Fermi-Dirac distribution is $f(E_n(\mathbf{k}))=1/\{1+[E_n(\mathbf{k})-\mu(T)]/k_BT\}$, where k_B is the Boltzmann constant and $\mu(T)$ is the temperature-dependent chemical potential. The energy width Γ comes from various deexcitation mechanisms. Both intralayer polarizations ($P_{11}^{(1)}=P_{22}^{(1)}$) and interlayer polarizations ($P_{12}^{(1)}=P_{21}^{(1)}$) make contributions to the dynamic charge screening. For the former and latter, the excited electrons and holes due to the dynamic Coulomb potentials are, respectively, located on the same and different layers. The interlayer polarizations are caused by the interlayer atomic hopping integrals. They are neglected in the previous studies on the semiconductor superlattices.

The effective potentials in Eq. (7) are related to the loss function which characterizes the intrinsic excitation properties. The probing electrons would transfer momentum and

energy $(\mathbf{q}, \omega)$ to the bilayer graphites. The inelastic scattering probability is proportional to the loss function or the screened response function. By detailed calculations, the loss function obtained from Fermi's golden rule is defined as

$$\text{Im}[-1/\epsilon] \equiv \sum_{l} \text{Im}\left[-V_{ll}^{eff}(\mathbf{q},\omega)\right] \Bigg/ \left(\sum_{ll'} V_{ll'}(q)/2\right).$$

$$(10)$$

The denominator is the average value of the external potentials on two layers. The loss function in Eq. (10) would be used to investigate the screened excitation properties.

III. π-ELECTRONIC EXCITATIONS

We first see the low-frequency excitation properties of the AA-stacked bilayer graphite. The single-particle excitations are characterized by the imaginary parts of the bare response functions. Im $P_{11}^{(1)}$ [Fig. 3(a)] must be positive because of the law of causality. However, the interlayer tunneling effect causes Im $P_{12}^{(1)}$ to be positive or negative [Fig. 3(b)]. The four linear energy bands, as shown in the inset of Fig. 2(a), could induce nine kinds of single-particle excitations: $\pi_1^* \rightarrow \pi_1^*$, $\pi_1 \rightarrow \pi_1$, $\pi_1^* \rightarrow \pi_1$, $\pi_1 \rightarrow \pi_1^*$, $\pi_2 \rightarrow \pi_2^*$, $\pi_2 \rightarrow \pi_1^*$, $\pi_1^* \rightarrow \pi_2^*$, $\pi_1 \rightarrow \pi_2^*$, and $\pi_2 \rightarrow \pi_1$. The two former are the intraband excitations, and the others are the interband excitations. The first four kinds of single-particle excitations exhibit a square-root divergence in Im $P_{11}^{(1)}$ and Im $P_{12}^{(1)}$ [Fig. 3(b)] at the lower frequency $\omega_{sp}^1 = 3\alpha_0 bq/2$ [Eq. (2)]. This special structure is caused by the excitation from the occupied $\mathbf{k_F}$ state of the π_1^* band (or the π_1 band) to the unoccupied $\mathbf{k_F} + \mathbf{q}$ state of the π_1^* band (or the π_1 band).[15] The $\pi_2 \rightarrow \pi_2^*$ interband excitations do not display any special structure, mainly due to the absence of Fermi-momentum states in two energy bands. The others exhibit two square-root divergences at $\omega_{sp}^{2,3} = 2\alpha_1 \mp 3\alpha_0 bq/2$. From the Kramers-Kronig relations, the real parts of the bare response functions also diverge in the square-root form.

The stacking sequence significantly affects the energy bands and thus the low-frequency electron-hole (e-h) excitations. The AB-stacked bilayer graphite has two pairs of valence bands and conduction bands [inset in Fig. 2(b)]. Each pair of parabolic energy bands exhibits a special discontinuous structure (a logarithmic divergence) in the imaginary (real) part of the bare response function [Figs. 3(c) and 3(d)]. The discontinuity is associated with the local minimum or maximum of the 2D parabolic energy dispersion in the energy-wave-vector space;[31] that is, it arises from the interband excitations of the band-edge states in the parabolic bands. There are two important differences between the AB- and AA-stacked bilayer graphites in the low-frequency e-h excitations. The former exhibits discontinuities, but not the square-root divergences. That energy dispersions are parabolic or linear determines this difference. Its e-h excitations are relatively weak, as compared with those of the latter. The lower the free carrier density is, the weaker the excitation strength is.

The loss function is useful in understanding the collective excitations and the measured excitation spectra from EELS.
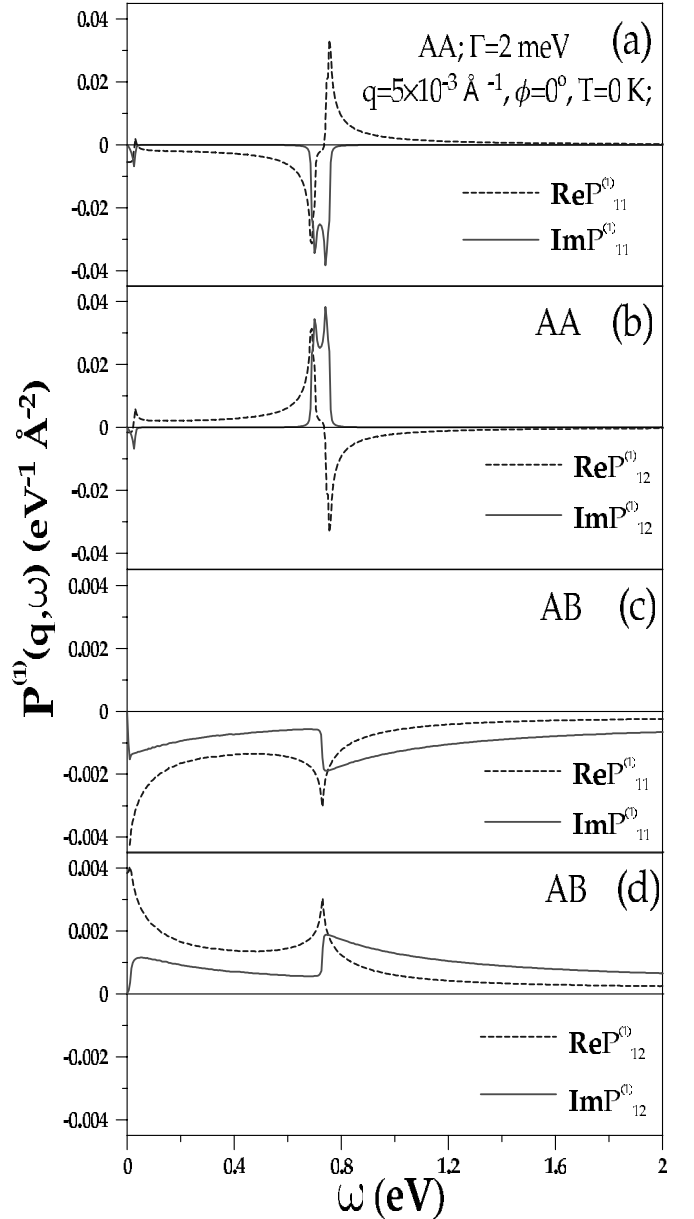

FIG. 3. (a) The intralayer and (b) interlayer response functions of the AA-stacked system at the low frequency and those of the AB-stacked system shown in (c) and (d).

The screened excitation spectra of the AA-stacked system are shown in Fig. 4(a) for various q's and $\phi = 0°$. They might display three prominent peaks. The second peak exists only when the transferred momentum is sufficiently high [the inset in Fig. 4(a)]. Such peaks are identified as the collective excitations of the free carriers in the linear bands. The low-frequency plasmons are related to the strong interband e-h excitations at ω_{sp}^1, ω_{sp}^2, and ω_{sp}^3. The first plasmon is due to $(\pi_1^* \rightarrow \pi_1^*, \pi_1^* \rightarrow \pi_1, \pi_1 \rightarrow \pi_1, \pi_1 \rightarrow \pi_1^*)$, and the other two plasmons result from $(\pi_2 \rightarrow \pi_1^*, \pi_1^* \rightarrow \pi_2^*, \pi_1 \rightarrow \pi_2^*; \pi_2 \rightarrow \pi_1)$. The intensity of the first plasmon peak declines in increments of the transferred momentum, while the opposite is true for the second plasmon peak. As to the third plasmon peak, its intensity grows and then decreases.
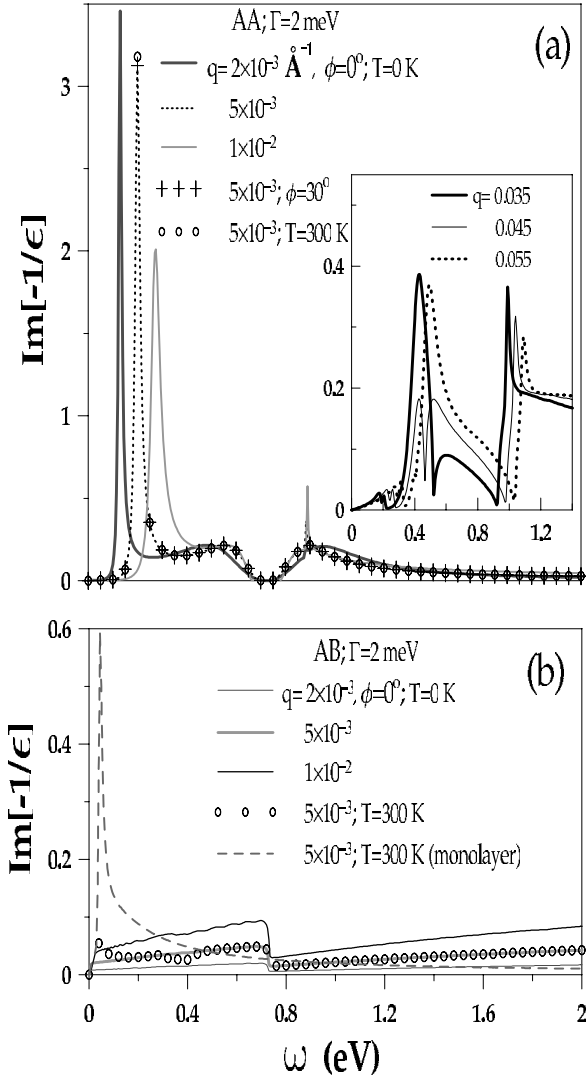
FIG. 4. The low-frequency loss spectra of the (a) AA- and (b) AB-stacked graphites at $\Gamma=2$ meV, $T=0$, $\phi=0°$, and different q's. Those at (a) $\phi=30°$, (a) $T=300$ K, or (b) $T=300$ K are also calculated. The inset of (a) shows those at larger q's. The loss spectrum of a monolayer graphite is shown at (b) $T=300$ K.
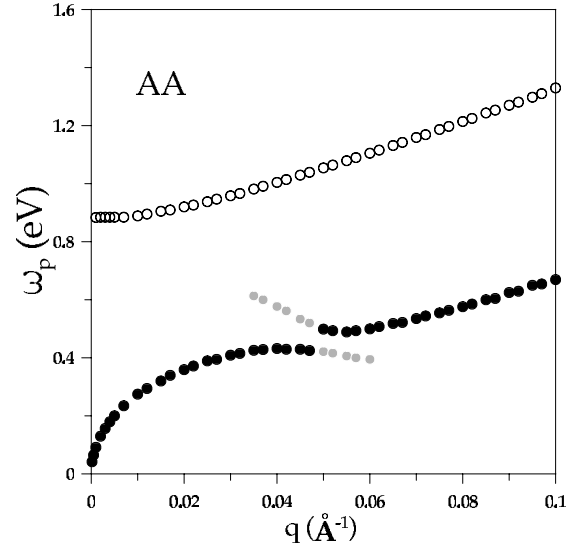

FIG. 5. The momentum-dependent frequencies of the low-frequency plasmons in the AA-stacked system. The light solid circles correspond to the weak plasmon peaks in the loss spectra.

The low-frequency loss spectra of the AA-stacked system are hardly affected by the direction of the transferred momentum and the temperature. The low-energy bands are nearly isotropic and so are the loss spectra. For example, the loss spectrum at $\phi=0°$ is almost identical to that at $\phi=30°$ [the dashed and crossed curves in Fig. 4(a)]. The temperature would alter the carrier occupation number near the Fermi level; therefore, it might affect four kinds of single-particle excitations associated with the π_1^* and π_1 bands. The original single-particle excitations are reduced by the temperature, owing to the partially occupied states above the Fermi level [Eq. (9)]. On the other hand, there are additional single-particle excitations from the partially unoccupied states below the Fermi level. Such excitations would cancel out the previous loss. That the single-particle excitation energies and the Coulomb matrix elements due to the linear bands remain unchanged accounts for the cancellation. As a result, the

plasmon peaks are almost independent of temperature (the dashed and circled curves).

The low-frequency excitation spectra are very sensitive to the changes in the stacking sequence and the interlayer atomic interactions. The AB-stacked system does not exhibit prominent plasmon peaks, as shown in Fig. 4(b). The free carrier density is too low to induce the collective excitations. The temperature could produce some free carriers, while the low-frequency plasmons are absent at room temperature (the circled curve). The AB-stacked system, the AA-stacked system, and the monolayer system quite differ from one another in temperature dependence, since purely temperature-induced plasmons only exist in the last system (the dashed curve).[17] This important difference clearly illustrates that the low-energy physical properties are dominated by the interlayer atomic interactions and the stacking sequence.

The transferred momentum determines the main features of the low-frequency plasmons in the AA-stacked system. The plasmon frequencies ω_p's strongly depend on q, as shown in Fig. 5. Plasmons are quanta of the electron density oscillations. Here the strong dispersion relation of plasmon frequency with q means that the plasma oscillation behaves as a propagating wave with wavelength $2\pi/q$ and group velocity $d\omega_p(q)/dq$. The frequency of the first plasmon grows quickly as q increases from zero. And then, it decreases with a further increase of q. $\omega_p(q)$ is well fitted by $\sqrt{q}$ at small q. The first plasmon belongs to an acoustic plasmon, and the q-dependent behavior is similar to that of a 2D electron gas. On the other hand, at large q, the first plasmon is absent or merges into the second plasmon [the inset in Fig. 4(a)]. The second plasmon cannot survive at small q, since it is seriously damped by the single-particle excitations corresponding to the third plasmon. As to the third plasmon, its frequency at $q\rightarrow0$ is higher than the single-particle excitation energy, $2\alpha_1$. The third plasmon is an optical plasmon, and it behaves as a 3D electron gas.

The high-frequency electronic excitations are dominated by the electronic states near the M point [Figs. 2(a) and
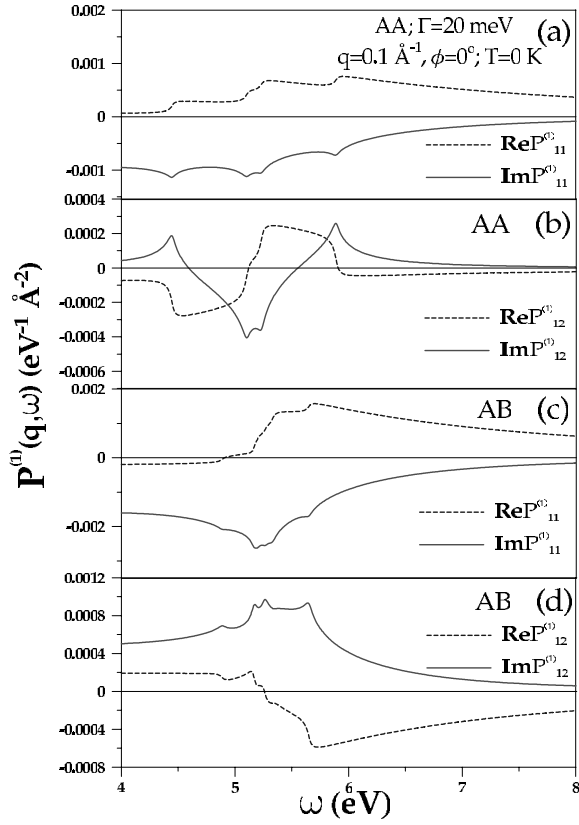
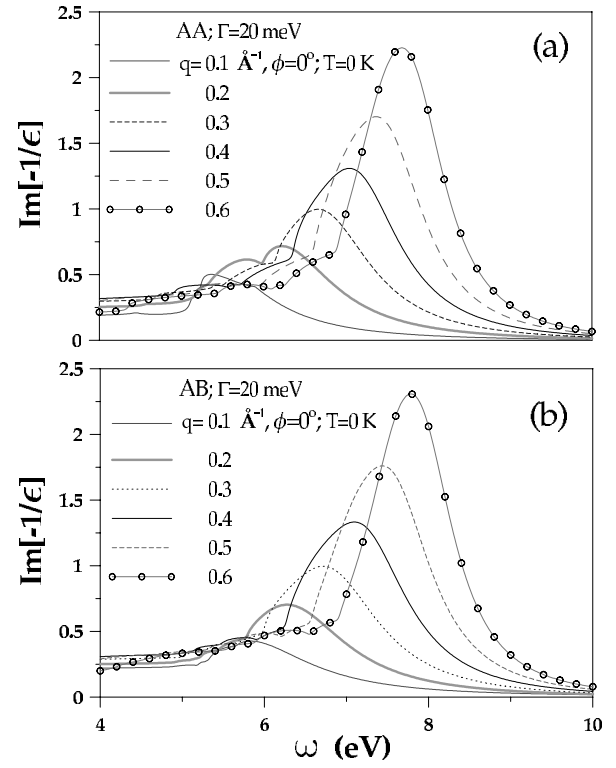FIG. 6. Same plot as Fig. 3, but shown at high frequency.

FIG. 7. The high-frequency loss spectra of the (a) AA- and (b) AB-stacked graphites at $\Gamma = 20$ meV, $T = 0$, $\phi = 0°$, and different q's.

2(b)]. The two occupied π_1 and π_2 bands have the parabolic energy dispersions and so do the two unoccupied π_1^* and π_2^* bands. These parabolic bands cause four kinds of single-particle excitations: $\pi_1 \to \pi_1^*$, $\pi_1 \to \pi_2^*$, $\pi_2 \to \pi_1^*$, and $\pi_2 \to \pi_2^*$. The single-particle response functions, as shown in Figs. 6(a)–6(d), would exhibit four logarithmic divergences (discontinuous structures) in the imaginary (real) part. Such special structures come from the saddle points near the M point.[31] They would, respectively, happen at frequencies lower and larger than $2\alpha_0$. The fourth special structure, which corresponds to the $\pi_2 \to \pi_2^*$ excitations occurs at the highest frequency. The energy difference between two special structures is larger in the AA-stacked system, as compared with that in the AB-stacked system. This result further illustrates that the AA-stacked system has the stronger interlayer atomic interactions and it would be reflected in the loss function. The single-particle excitations are very different in the high- and low-frequency ranges [Figs. 3 and 6], such as the excitation channels and the special structures in $P_{ll'}^{(1)}$. The main differences are determined by energy dispersions (parabolic or linear) and critical points (saddle points, minima, or maxima) near the M and K points.

The high-frequency loss functions are, respectively, shown in Figs. 7(a) and 7(b) for the AA- and AB-stacked systems at various q's and $\phi = 0°$. A very prominent peak, identified as the π plasmon, is present in each loss spectrum. This peak is associated with the fourth special structure in the single-particle response functions [the $\pi_2 \to \pi_2^*$ excitation in Figs. 6(a)–6(d)]. The π plasmon corresponds to the collective excitations of all the π electrons. The similar π plas-

mon could also be found in the graphite-related materials—e.g., carbon fullerenes[32] and carbon nanotubes.[6] There also exist few less prominent peaks or shoulder structures in the loss functions. Such structures are closely related to the $\pi_1 \to \pi_1^*$, $\pi_1 \to \pi_2^*$, and $\pi_2 \to \pi_1^*$ excitations, since they happen at the frequencies close to the single-particle excitation energies. They could be regarded as interband plasmons, as observed in carbon nanotubes.[6] The dependence of their frequencies on momentum is difficult to identify from the excitation spectra. In general, the loss spectra are dominated by the π plasmon but not the interband plasmons.

The momentum-dependent π-plasmon frequency is shown in Fig. 8. ω_p grows quickly as q increases. This result responds directly to the characteristic of energy bands, the strong wave-vector dependence. At the long-wavelength limit $q \to 0$, the π-plasmon frequency of the AA-stacked system is $\omega_p \sim 2(\alpha_0 + \alpha_1)$ (the solid circles). Its value is close to the maximum single-particle excitation energy from the M point [Eq. (2)]. The finite frequency means that the π plasmon is an optical plasmon. The AB- and AA-stacked systems exhibit the similar π plasmons. The only difference is that the former has the lower plasmon frequency at small q (the open diamonds). Such a difference comes from the weaker interlayer atomic interactions in the AB-stacked system. When the interlayer atomic interactions are neglected, the π-plasmon frequency is largely reduced at small q (the solid triangles) and ω_p at $q \to 0$ is almost identical to that of a monolayer graphite (the open circles). These two results clearly illustrate that the interlayer atomic interactions or the energy bands determine the π-plasmon frequency at small q. As to the interlayer Coulomb interactions, they could make
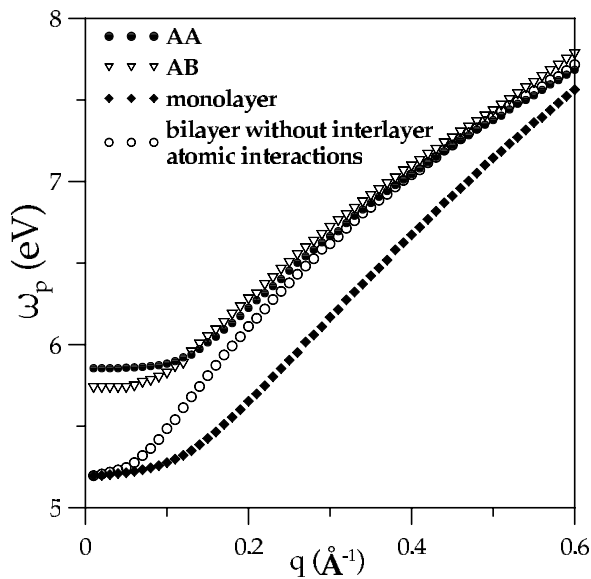
FIG. 8. The momentum-dependent π-plasmon frequencies of the (a) AA- and (b) AB-stacked graphites. Also shown are those without the interlayer atomic interactions, or those of a monolayer graphite.

important contributions to the π-plasmon frequency at large q. The plasmon frequency is greatly enhanced by the Coulomb coupling of the π-electron oscillations in two layers.

The AB-stacked bulk graphite contrasts sharply with the AB-stacked bilayer graphite in collective excitations. The low-frequency optical plasmons, with ω_p's smaller than 0.2 eV, exist in the former[3–5,18] but not the latter. The AB-stacked bulk graphite owns the 3D bare Coulomb potential $v_q = 4\pi e^2/q^2$. The very strong Coulomb potential at $q \to 0$ is responsible for the existence of the low-frequency plasmons.[18] At small q, the π-plasmon frequency [>6.5 eV (Refs. 6–9)] of the former is higher than that (~ 5.7 eV) of the latter. The energy difference between the π_2 and π_2^* bands near the M point is larger in the AB-stacked bulk graphite [Fig. 1b in Ref. 33 and Fig. 2(b)] and so are the single-particle excitation energy and the π-plasmon frequency.

IV. CONCLUDING REMARKS

In this work, the π-electronic excitations of the AA- and AB-stacked bilayer graphites are studied within the linear SCF method. The interlayer atomic interactions and the interlayer Coulomb interactions are included in the calculations simultaneously. The single-particle response functions directly reflect the main features of energy bands. Their special structures and excitation energies are determined by energy dispersions and critical points. The loss spectra strongly depend on the stacking sequence, the interlayer atomic interactions, the interlayer Coulomb interactions, and the magnitude of the transferred momentum. However, they are hardly affected by the direction of the transferred momentum and the temperature. EELS and optical experiments could be used to verify the predicted loss spectra and plasmon frequencies.

There exist three low-frequency plasmon modes in the AA-stacked system but not the AB-stacked system. The AA- and AB-stacked plasmons exhibit similar π plasmons. The first low-frequency plasmon is an acoustic plasmon, and the others are optical plasmons. The main differences between these two kinds of plasmons include the frequency, the momentum dependence, and the intensity of spectrum. The bilayer graphites are very different from the monolayer graphite and the AB-stacked bulk graphite in the existence of the low-frequency plasmons and the π-plasmon frequency at small momentum. The important differences among the different graphitic systems clearly illustrate that interlayer atomic interactions and interlayer Coulomb interactions dominate over electronic excitations.

This work shows that the stacking sequence or the symmetric configuration dominates the band structures near the Fermi level and thus the low-frequency Coulomb excitations. It could be deduced that the symmetric configuration plays an important role on the Coulomb excitations of double-walled carbon nanotubes. From previous studies of electronic and optical properties,[34,35] metallic double-walled carbon nanotubes are expected to exhibit several low-frequency plasmons. These plasmons would be quite different from those of the bilayer graphite, mainly owing to the cylindrical symmetry and the lower dimensionality.[36]

[1] J. M. D. Coey, M. Venkatesan, C. B. Fitzgerald, A. P. Douvalis, and I. S. Sanders, Nature (London) **420**, 156 (2002).

[2] A. Hashimoto, K. Suenaga, A. Gloter, K. Urita, and S. Iijima, Nature (London) **430**, 870 (2004).

[3] E. T. Jensen, R. E. Palmer, W. Allison, and J. F. Annett, Phys. Rev. Lett. **66**, 492 (1991).

[4] P. Laitenberger and R. E. Palmer, Phys. Rev. Lett. **76**, 1952 (1996).

[5] H. Venghaus, Phys. Status Solidi B **81**, 221 (1977).

[6] T. Pichler, M. Knupfer, M. S. Golden, J. Fink, A. Rinzler, and R.

E. Smalley, Phys. Rev. Lett. **80**, 4729 (1998).

[7] K. Zeppenfeld, Z. Phys. **243**, 229 (1971).

[8] U. Buchner, Phys. Status Solidi B **81**, 227 (1977).

[9] E. A. Taft and H. R. Philip, Phys. Rev. **138**, A197 (1965).

[10] H. Kempa, P. Esquinazi, and Y. Kopelevich, Phys. Rev. B **65**, 241101 (2002).

[11] Y. Zhang, J. P. Small, M. E. S. Amori, and P. Kim, Phys. Rev. Lett. **94**, 176803 (2005).

[12] P. R. Wallace, Phys. Rev. **71**, 622 (1947).

[13] J. C. Charlier, J.-P. Michenaud, X. Gonze, and J.-P. Vigneron,

Phys. Rev. B **44**, 13237 (1991).

[14] J. C. Charlier, J.-P. Michenaud, and X. Gonze, Phys. Rev. B **46**, 4531 (1992).

[15] Kenneth W.-K. Shung, Phys. Rev. B **34**, 979 (1986).

[16] M. F. Lin and Kenneth W.-K. Shung, Phys. Rev. B **53**, 1109 (1996).

[17] F. L. Shyu and M. F. Lin, J. Phys. Soc. Jpn. **69**, 607 (2000).

[18] F. L. Shyu and M. F. Lin, J. Phys. Soc. Jpn. **69**, 3781 (2000).

[19] E. J. Duplock, M. Scheffler, and P. J. D. Lindan, Phys. Rev. Lett. **92**, 225502 (2004).

[20] V. P. Gusynin and S. G. Sharapov, Phys. Rev. Lett. **95**, 146801 (2005).

[21] F. Ortmann, W. G. Schmidt, and F. Bechstedt, Phys. Rev. Lett. **95**, 186101 (2005).

[22] K. S. Novoselov, A. K. Geim, S. V. Morozov, D. Jiang, Y. Zhang, S. V. Dubonos, I. V. Grigorieva, and A. A. Firsov, Science **306**, 666 (2004).

[23] J. S. Bunch, Y. Yaish, M. Brink, K. Bolotin, and P. L. McEuen, Nano Lett. **5**, 287 (2005).

[24] C. Berger, Z. Song, T. Li, X. Li, A. Y. Ogbazghi, R. Feng, Z. Dai, A. N. Marchenkov, E. H. Conrad, P. N. First, and W. A. de Heer, J. Phys. Chem. B **108**, 19912 (2004).

[25] Y. Zhang, Y. W. Tan, H. L. Stormer, and P. Kim, Nature (London) **438**, 201 (2005).

[26] K. S. Novoselov, A. K. Geim, S. V. Morozov, D. Jiang, M. I. Katsnelson, I. V. Grigorieva, S. V. Dubonos, and A. A. Firsov, Nature (London) **438**, 197 (2005).

[27] M. Fujita, K. Wakabayashi, K. Nakada, and K. Kusakabe, J. Phys. Soc. Jpn. **65**, 1920 (1996).

[28] M. Fujita, M. Igami, and K. Nakada, J. Phys. Soc. Jpn. **66**, 1864 (1997).

[29] M. S. Dresselhaus and G. Dresselhaus, Adv. Phys. **30**, 139 (1981).

[30] H. Ehrenreich and M. H. Cohen, Phys. Rev. **115**, 786 (1959).

[31] L. Van Hove, Phys. Rev. **89**, 1189 (1953).

[32] G. Gensterblum, J. J. Pireaux, P. A. Thiry, R. Caudano, J. P. Vigneron, Ph. Lambin, and A. A. Lucas, Phys. Rev. Lett. **67**, 2171 (1991).

[33] C. P. Chang, C. L. Lu, F. L. Shyu, R. B. Chen, and M. F. Lin, Carbon **43**, 1424 (2005).

[34] Y. H. Ho, C. P. Chang, F. L. Shyu, S. C. Chen, and M. F. Lin, Carbon **42**, 3159 (2004).

[35] G. W. Ho, Y. H. Ho, T. S. Li, C. P. Chang, and M. F. Lin, Carbon **44**, 2323 (2006).

[36] Y. H. Ho *et al.* (unpublished).